

Relativistic van Allen belts in magnetospheres of pulsars and white dwarfs

Maxim V. Barkov^a and Maxim Lyutikov^b

^aInstitute of Astronomy, Russian Academy of Sciences,
Moscow, 119017 Russia

^bDepartment of Physics and Astronomy, Purdue University,
525 Northwestern Avenue, West Lafayette, IN 47907-2036, USA

E-mail: barkov@inasan.ru

Abstract. We consider dynamics and multi-frequency emission patterns of relativistic van Allen belts - particles trapped in the magnetospheres of neutron stars and White Dwarfs. We account for synchrotron radiative losses and effects of relativistic beaming of radiation. The system is non-Hamiltonian (non-energy conserving): this results in a wide non-scalable variety of spectral and temporal behaviors. There are three types of trapped particles' trajectories: (i) oscillating (particles experience multiple bounces between magnetic bottles); (ii) precipitating (particles fall onto the star with finite transverse momentum); (iii) freezing (particles lose their transverse motion before falling onto the star). The separation between regimes (i) and (ii) depends both on the ratio of the bounce time to cooling time at magnetic equator τ_0 , $\eta_0 = R_0/(c\tau_0) \leq 1$, as well as the initial pitch angle α_0 ; regimes (i) and (ii) are separated at $\alpha_{0,crit} \sim \eta_0^{3/10}$. Resulting emission patterns show large variety: single or double peaked, and/or flat hat with sharp walls. Multi-frequency profiles - in optical and X-ray bands - can be used to get information about physical (magnetic field strength, injection point) and geometrical (dipolar angle and the line of sight) properties.

¹Corresponding author.

Contents

1	Relativistic van Allen belts in astrophysical high energy sources	1
2	Radiative and adiabatic forces for trapped particles	2
2.1	Radiative damping	3
2.2	Adiabatic forces	4
2.3	Dipolar field	5
3	Particle trajectories and synchrotron emission patterns	6
3.1	Method	6
3.2	Particle trajectories: bouncing, freezing and precipitation	7
3.3	Injection procedure and emissivity	9
3.4	Emission patterns and spectra	10
4	Applications and discussion	13

1 Relativistic van Allen belts in astrophysical high energy sources

A number of highly unusual compact binary systems show a presence of relativistic particles trapped in the magnetospheres - astrophysical analogs of the terrestrial and Jovian van Allen belts. These systems include the double pulsar companion PSR J0737-3039B, low states of transitional millisecond pulsars like PSR J1023+0038, as well as two exceptional magnetic white dwarfs in cataclysmic variables AE Aqr and AR Sco. In all these systems, there is clear evidence of magnetohydrodynamic interactions between stellar winds/accretion flow and the magnetosphere of the primary. The systems show non-thermal emission, extending from radio to optical to X-rays, and in some cases to γ -rays. Emitting relativistic particles are likely accelerated during magnetic reconnection events at the magnetospheric boundary. All these systems represent exotic paths/stages of binary evolution.

Van Allen radiation belts in the Earth magnetosphere [*e.g.* 1] are zones of energetic charged particles captured from the solar wind (the Inner Van Allen radiation belt, consisting mainly of energetic protons, is the product of the decay of so-called "albedo" neutrons). They were one of the first Solar wind charged particles observed at the Earth; understanding them played a major role in the development of space science and plasma (astro)physics [2]. Recent observations of compact astrophysical high energy sources indicate a presence of similar population in interacting neutron stars and White Dwarfs binaries. These include a presence of dense plasma on the closed field lines of the double pulsar PSR J0737-3039B [3], particles producing high energy emission in highly asynchronous polars AR Sco and AE Aqr [4–6], and low states states of transitional millisecond pulsars [7, 8].

There are a number of principal differences between terrestrial (and Jovian) van Allen belts and those expected in astrophysical compact objects like neutron stars and White Dwarfs: in astrophysical high energy sources radiative losses are/can be important (in the case of planetary magnetospheres, the most important loss processes are collisions with neutrals). In addition terrestrial plasma is mildly collisional: interaction of high energy particles with the neutral components is one of the dominant effects. In contrast, astrophysical plasma is highly collisionless. The plasma parameters in astrophysical sources are expected to be very

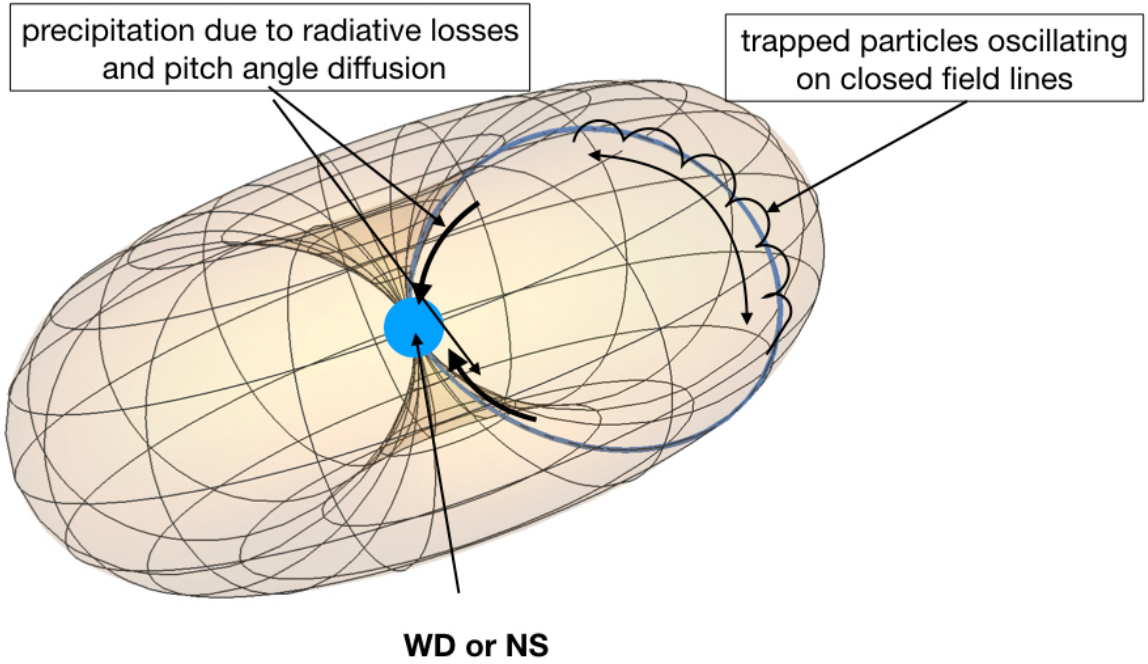


Figure 1. Dynamic of relativistic particles trapped in the magnetospheres of whites dwarfs/neutron stars. Injected particles experience adiabatic reflections between magnetic poles, lose energy to synchrotron radiation, and experience pitch angle scattering due to interaction with the turbulence.

different from the near space plasmas: in neutron stars plasma is expected to be magnetically dominated, and composed of electron-positron pairs. Both these effects change qualitatively the normal models of plasma and wave-particle interaction (*e.g.*, there are no whistler modes in pair plasma).

2 Radiative and adiabatic forces for trapped particles

The particles comprising terrestrial van Allen belts are held trapped for a long time due to the conservation of first adiabatic invariant (magnetic bottling effect), Fig 1. The particles experience periodic motion between the magnetic poles, repulsed from the regions of strong magnetic fields. The dominant non-adiabatic effects are pitch angle diffusion rates due to Coulomb collisions, non-elastic collisions with neutral and resonant interactions with wave turbulence [*e.g.* 1, 9–12].

In relativistic magnetospheres a new effect appears: radiative damping of cyclotron motion. Analysis of corresponding trajectories and emission patterns is the main goal of the present work. Thus, the two main effects that control particle dynamics are conservation of the first adiabatic invariant and radiative losses.

Conservation of the first adiabatic invariant may in fact be expressed in terms of effective forces \mathbf{F}_{ad} , while radiative damping can be expressed in terms of radiative force \mathbf{F}_{rad} . We consider them next for a relativistic particle moving an inhomogeneous magnetospheric magnetic field with Lorentz factor γ and pitch angle α .

2.1 Radiative damping

Consider a particle moving in magnetic field with pitch angle α , so that velocities perpendicular and along the magnetic field are

$$\begin{aligned} v_{\perp} &= c\beta \sin \alpha \\ v_{\parallel} &= c\beta \cos \alpha \end{aligned} \quad (2.1)$$

The radiation reaction force can be written as [13, parag 76]

$$\begin{aligned} F_{\perp} &= -\frac{2\beta B^2 e^4 \sin \alpha (1 + \beta^2 \gamma^2 \sin^2(\alpha))}{3c^4 m_e^2} = -\beta \sin \alpha (1 + \beta^2 \gamma^2 \sin^2 \alpha) \frac{m_e c}{\tau_c} \\ F_{\parallel} &= -\frac{2\beta^3 B^2 \gamma^2 e^4 \sin^2 \alpha \cos(\alpha)}{3c^4 m_e^2} = -\beta^3 \gamma^2 \sin^2 \alpha \cos \alpha \frac{m_e c}{\tau_c} \\ \tau_c &= \frac{3c^5 m_e^3}{2B^2 e^4} \end{aligned} \quad (2.2)$$

Change of energy follows from

$$\begin{aligned} \partial_t(\gamma^2 - p^2) &= 0 \rightarrow \partial_t \gamma = \mathbf{v} \cdot \partial_t \mathbf{p} = \mathbf{v} \cdot \mathbf{F} \\ \frac{d\gamma}{dt} &= \frac{\mathbf{F}_{rad} \cdot \mathbf{v}}{m_e c^2} = -\frac{\gamma^2 \beta^2 \sin^2 \alpha}{\tau_c} \end{aligned} \quad (2.3)$$

The momentum equation $\partial_t \mathbf{p} = \mathbf{F}_{rad}$ then gives

$$\frac{d\alpha}{dt} = -\frac{\sin(2\alpha)}{2\gamma\tau_c} \quad (2.4)$$

Combing (2.3) and (2.4) we find

$$\frac{d\gamma}{d\alpha} = \gamma^3 \beta^2 \tan \alpha \quad (2.5)$$

with solution

$$\begin{aligned} \beta\mu &= \beta_0\mu_0 \\ \mu &= \cos \alpha \end{aligned} \quad (2.6)$$

where β_0 and α_0 are initial velocity and pitch angle. Thus, parallel velocity $\beta \cos \alpha$ and parallel Lorentz factor remains constant

$$\gamma_{\parallel} = \frac{1}{\sqrt{1 - \beta^2 \mu^2}} = \text{const} \quad (2.7)$$

Temporal evolution of Lorentz factor is given by

$$\gamma = \gamma_{\parallel} \coth \left(\frac{t}{\gamma_{\parallel} \tau_c} + \text{arccoth}(\gamma_0/\gamma_{\parallel}) \right) \quad (2.8)$$

This generalizes the known case with no parallel motion

$$\gamma_{\perp} = \coth(t/\tau_c + \text{arccoth}\gamma_{\perp,0}) \quad (2.9)$$

Relation (2.8) can also be derived from (2.9) using Lorentz transformation for time and noting that $\gamma = \gamma_{\parallel}\gamma_{\perp}$. Interestingly, though there is axial force, the axial velocity remains constant.

Evolution of pitch angle follows from (2.6) and (2.8):

$$\mu = \frac{\beta_0\mu_0}{\sqrt{1 - \frac{\coth^2\left(\frac{t}{\gamma_{\parallel,0}\tau c} + \tanh^{-1}\left(\frac{\gamma_0}{\gamma_{\parallel,0}}\right)\right)}{\gamma_{\parallel,0}^2}}} \quad (2.10)$$

As $t \rightarrow \infty$, $\mu \rightarrow 1$.

After losing all the transverse momentum, $\alpha = 0$, the particle is left with velocity

$$\beta_f = \beta_0 \cos \alpha_0 \quad (2.11)$$

and final energy

$$\gamma_f = \gamma_{\parallel} \quad (2.12)$$

The additional radiation reaction force comes from curvature emission

$$F_{\parallel,curv} = -\frac{2\gamma^4 e^2}{3R_c^2} \quad (2.13)$$

where R_c is the curvature radius.

For curvature emission to become important, the Lorentz factor should be extremely high,

$$\gamma \geq \sqrt{c\omega_B/R_c} \quad (2.14)$$

We assume that this regime is not achievable and neglect curvature emission.

2.2 Adiabatic forces

As a particle moves in inhomogeneous magnetic field it conserves energy and the first adiabatic invariant. As a result,

$$\sin \alpha = \sqrt{\frac{B}{B_0}} \sin \alpha_0. \quad (2.15)$$

We can then formulate adiabatic force as

$$\begin{aligned} G_{\perp} &= \pm \frac{\beta^2 \gamma m_e c^2}{4} \frac{(\mathbf{b}\nabla)B}{B} \sin 2\alpha \\ G_{\parallel} &= \mp \frac{\beta^2 \gamma m_e c^2}{2} \frac{(\mathbf{b}\nabla)B}{B} \sin^2 \alpha \end{aligned} \quad (2.16)$$

where \mathbf{b} is unit vector along the magnetic field and upper (lower) signs correspond to particle propagating towards (away from) the regions of increasing magnetic field. Note that the expression $((\mathbf{b}\nabla)B)/B$ is *not* the curvature of field lines, which is $(\mathbf{b}\nabla)\mathbf{b}$.

Since $\mathbf{G} \cdot \mathbf{v} = 0$, $\gamma = \text{const}$ we can write the pitch angle evolution as

$$\partial_t \alpha = \pm \frac{(\mathbf{b}\nabla)B}{2B} c \beta \sin \alpha. \quad (2.17)$$

For particles propagating towards the star, radiative and adiabatic forces oppose each other in the evolution of the pitch angle. Which force “wins” depends in a subtle way on the

parameters of the system and the injection location - this make this simple system exceptional rich.

Qualitative, estimating $((\mathbf{b}\nabla)B)/B \sim 1/L_B$, the ratio fo adiabatic and radiative forces

$$\begin{aligned}\frac{G_{\perp}}{F_{\perp}} &\approx \frac{\beta\gamma \cos \alpha}{1 + \beta^2\gamma^2 \sin^2 \alpha} \times \frac{c\tau_c}{L_B} \\ \frac{G_{\parallel}}{F_{\parallel}} &\approx \frac{1}{\beta\gamma \cos \alpha} \times \frac{c\tau_c}{L_B}\end{aligned}\quad (2.18)$$

For not very small pitch angles, $\alpha \geq 1/\gamma$,

$$\frac{G}{F} \approx \frac{c\tau_c}{\gamma L_B} \quad (2.19)$$

2.3 Dipolar field

Next we specify previous relations to the case of dipolar fields. A field line which reaches R_0 at magnetic equator is given by

$$\begin{aligned}\frac{r}{R_0} &= \sin^2 \theta \\ B &= \sqrt{\sin^2 \theta + 4 \cos^2 \theta} \left(\frac{R_0}{r}\right)^3 B_0 = \\ &= \sqrt{4 - 3\frac{r}{R_0}} \left(\frac{R_0}{r}\right)^3 B_0 \\ ds &= R_0 \sin \theta \sqrt{\sin^2 \theta + 4 \cos^2 \theta} d\theta \\ ((\mathbf{b}\nabla)B)/B &= -\frac{3(27 \cos(\theta) + 5 \cos(3\theta))}{\sqrt{2}r(3 \cos(2\theta) + 5)^{3/2}}\end{aligned}\quad (2.20)$$

(ds is length along a given field line). We assumed that R_0 is the equatorial extension of a field line, $\theta_0 = \pi/2$

In dipole field, a path along the field can be parametrized as

$$ds = c\beta \cos \alpha dt \quad (2.21)$$

Using Eqs. (2.20) and (2.21) we can find the evolution of the Lorentz factor and the pitch angle

$$\begin{aligned}\frac{d\gamma}{dt} &= -\frac{\beta^2\gamma^2 \sin^2 \alpha \csc^{12}(\theta) (\sin^2(\theta) + 4 \cos^2(\theta))}{\tau_{c,0}} \\ \frac{d\alpha}{dt} &= \pm \frac{3\beta c \sin \alpha (27 \cos \theta + 5 \cos(3\theta)) \csc^2 \theta}{2\sqrt{2}R_0(3 \cos(2\theta) + 5)^{3/2}} - \frac{\sin \alpha \cos \alpha \csc^{12}(\theta) (\sin^2(\theta) + 4 \cos^2(\theta))}{\gamma\tau_{c,0}} \\ \frac{d\theta}{dt} &= \mp \frac{\beta c \cos \alpha \csc^2 \theta}{R_0\sqrt{4 \cot^2 \theta + 1}}\end{aligned}\quad (2.22)$$

where $\tau_{c,0}$ is defined in terms of the magnetic field at R_0 .

Next we change to dimensionless quantities. We normalize time to

$$\tilde{t} = (ct)/R_0 \quad (2.23)$$

Another parameter is dimensionless cooling time at R_0 , τ_c

$$\eta_c = \frac{R_0}{\tau_{c,0}c} = \frac{2B_0^2 e^4 R_0}{3c^6 m_e^3} \quad (2.24)$$

and change of parameters $\tilde{r} = r/R_0$.

We find

$$\begin{aligned} \frac{d\gamma}{d\tilde{t}} &= -\eta_0 \gamma^2 \beta^2 \sin^2 \alpha (3 \cos(2\theta) + 5) \csc^{12}(\theta) \\ \frac{d\alpha}{d\tilde{t}} &= \pm \frac{3\beta \sin \alpha (27 \cos(\theta) + 5 \cos(3\theta)) \csc^2(\theta)}{2\sqrt{2}(3 \cos(2\theta) + 5)^{3/2}} - \eta_0 \frac{2 \sin \alpha \cos \alpha (4 \cot^2(\theta) + 1) \csc^{10}(\theta)}{\gamma} \\ \frac{d\theta}{d\tilde{t}} &= -\frac{\beta \cos(\alpha)}{\sin^2 \theta \sqrt{5 + 3 \cos(2\theta)}} \end{aligned} \quad (2.25)$$

This is a set of equations for particle's velocity and Lorentz factor, pitch angle α and location in the dipole magnetospheres θ .

For $\eta_c \geq 1$ (strongly cooling case) a particle just loses most of the energy at the furthest point. The case of slow cooling, $\eta_c \leq 1$ is more interesting, we assume this regime below.

Since we are interested in time-average state, the time differential can be replaced as

$$dt = \mp \frac{\sec \alpha \sqrt{4R_0 - 3r}}{2\beta c \sqrt{R_0 - r}} dr \quad (2.26)$$

Substituting Eq. (2.26) to Eq. (2.25) we get

$$\begin{aligned} \frac{d\gamma}{d\tilde{r}} &= -\eta_c \frac{\beta \gamma^2 (4 - 3\tilde{r})^{3/2} \sin \alpha \tan \alpha}{\sqrt{1 - \tilde{r}\tilde{r}^6}} \\ \frac{d\alpha}{d\tilde{r}} &= -\eta_c \frac{(4 - 3\tilde{r})^{3/2} \sin \alpha}{\beta \gamma \sqrt{1 - \tilde{r}\tilde{r}^6}} \mp \frac{3(8 - 5\tilde{r}) \tan \alpha}{4\tilde{r}(4 - 3\tilde{r})} \end{aligned} \quad (2.27)$$

The system of equations (2.27) is our main target: it describes the evolution of the energy and pitch angle for a particle experiencing synchrotron losses in dipolar magnetic field. Initial conditions can be chosen as given Lorentz factor γ_0 and pitch angle α_0 at the magnetic equator $\tilde{r} = 1$.

Since relations (2.27) are formally divergent near $\tilde{r} = 1$, for numerical integration to start near $\tilde{r} = 1$ one needs an analytical solution. At that point, there is no adiabatic term; we find

$$\begin{aligned} \gamma &\approx \gamma_0 - 2\gamma_0^2 \beta \eta_0 \sqrt{1 - \tilde{r}_0} \sin(\alpha_0) \tan(\alpha_0) \\ \alpha &\approx \alpha_0 - \frac{2\eta_c \sqrt{1 - \tilde{r}_0} \sin(\alpha_0)}{\beta \gamma_0} \end{aligned} \quad (2.28)$$

3 Particle trajectories and synchrotron emission patterns

3.1 Method

The system (2.27) is non-Hamiltonian (non-energy conserving). This results in a wide variety of behavior, typically not scalable one from another. As a result, to calculate the observed signal from trapped particles - the van Allen belts - a fairly complicated procedure is required:

(i) for each particle injected at a given point with a given pitch angle equations of motion should be integrated along dipolar magnetic field lines; (ii) the emission pattern (Doppler-boosted spectrum and direction in the observer frame) is then calculated; (iii) averaging over the initial distribution of pitch angles; (iv) averaging over the initial distribution of energies; (v) for different relative orientations of a dipole with respect to the companion wind, the injection will occur at different points in the magnetosphere.

Using standard Matlab procedures for stiff ordinary differential equations [ode15s from 14] with relative accuracy 10^{-7} , we numerically solve the set of equations Eq. (2.27) with $\eta_0 = 1.25 \times 10^{-4}$ (this value corresponds to AR Sco WD in the model of [6]) to calculate the evolution of Lorentz factor γ_e and pitch angle α along the particle trajectory.

We start particle motion from the magnetic dipole equatorial plane ($\tilde{r} = 1$) along a given magnetic field line. If a particle reaches the mirror point ($\alpha = \pi/2$) or injection point ($\tilde{r} = 1$), then we continue to calculate the trajectory until the particle loses 97% of the initial energy (only 3% of the initial energy left).

3.2 Particle trajectories: bouncing, freezing and precipitation

There are three types of particle trajectories: (i) bouncing: particle can experience multiple bounces between magnetic bottles near the pole (this is close to the conventional regime when the radiative losses are weak; (ii) precipitation: particles lose their transverse motion and fall onto the star; (iii) freezing particles lose most of their transverse and nearly all the parallel momentum, Fig. 2.

In case when both radiative damping and adiabatic forces are present, there is an interesting case which we call the “freezing” trajectory. Qualitatively, as a particle propagates towards regions of higher magnetic field, the adiabatic force acts to slow down parallel motion, and increase the transverse velocity. As result, a particle spends a lot of time near the reflection points, with large transverse momenta. Particles then experience large radiative losses; this is the “freezing” trajectory.

Let us approximate $(\mathbf{b}\nabla)B/B \sim 1/L_B$. A particle spends

$$\tau_B \sim L_B/c \quad (3.1)$$

near the reflection point. This is a region with largest magnetic field allowed by the first adiabatic invariant: a given particle spends a lot of time in the region with highest magnetic field. If radiative decay time at the reflection point is shorter than τ_B then a particle exponentially lose its energy and will not bounce back.

Estimating the reflection point as $\tilde{r} \sim \sin^{2/3} \alpha_0$, the freezing case corresponds to balancing two terms in the expression for α in (2.27):

$$\alpha_0 \sim \eta_c^{3/10} \quad (3.2)$$

For larger initial pitch angles particles experience bouncing trajectories, for smaller ones they precipitate.

To illustrate particle’s trajectories, we present nine solutions corresponding to a combination of initial pitch angle $\alpha_{e,0} = 0.005, 0.05, 0.5$ and $\gamma_{e,0} = 2 \times 10^3, 6 \times 10^3, 2 \times 10^4$. On the Fig. 2 we present radial dependence of the pitch angle (right) and Lorentz factor (center panel). To make trajectories more clear, we plot dependence of pitch angle from Lorentz factor. We can see three definite classes of trajectories: 1) large initial pitch angle leads to formation of “oscillation” trajectory; 2) the intermediate pitch angle leads to initial grow of

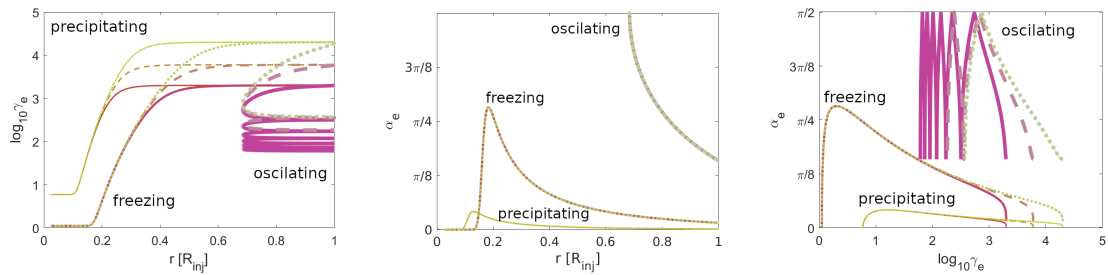


Figure 2. Left panel: radial dependence of electron Lorentz factor γ_e , Center panel: radial dependence of pitch angle α , Right Panel: trajectories of particles in the “pitch angle α -Lorentz factor γ_e ” plane. There are three types of trajectories: “oscillations” , “precipitation”, separated by a “freezing” trajectory. Particles are injected at $\tilde{r} = 1$ with different Lorentz factors and different pitch angles. The thin lines corresponds to $\alpha_{e,0} = 0.005$, the medium $\alpha_{e,0} = 0.05$ and thick ones $\alpha_{e,0} = 0.5$. The solid lines corresponds to $\gamma_{e,0} = 2 \times 10^3$, the dashed $\gamma_{e,0} = 6 \times 10^3$ and dotted $\gamma_{e,0} = 2 \times 10^4$. Particles with high initial pitch angle ($\gtrsim 0.1$) oscillate between reflection points with slowly decreasing energy. For sufficiently small pitch angles (~ 0.05) due to high radiative losses particle propagate deep into the magnetosphere, and quickly lose both parallel and perpendicular momentum. For even lower pitch angles ($\lesssim 0.01$) particle lose all the transverse energy and fall onto the star.

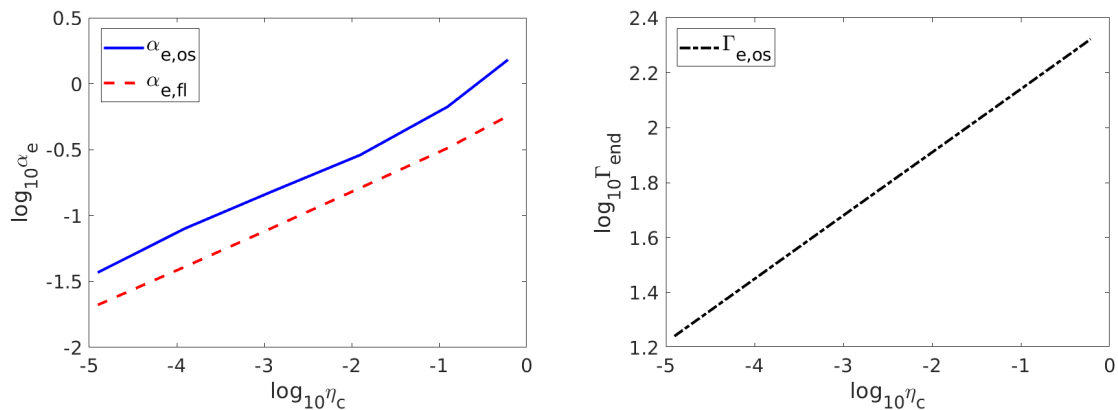


Figure 3. We plot data based on the Table 1. On the left panel, the maximal pitch angle of falling/“precipitation” trajectories depends on the η_0 parameter are presented by dashed line, the maximal pitch angle of the “frozen” trajectory presented by solid line. On the right panel is shown the logarithm of the maximal Lorentz factor of the falling particles by dot-dashed line.

pitch angle (up to value order of $\alpha_e \sim 1$) and cooling of Lorentz factor to 1 with collapse of pitch angle to 0, so called “frozen” trajectories; 3) the small pitch angles after moderate grow leads to collapse of pitch angle to 0 with $\gamma_e > 1$, so called “precipitation” or falling trajectories.

The analysis of the trajectories shows that the characteristic trajectory is determined by initial pitch angle. The particles with $\gamma_e > 10^2$ quickly lose energy and the latter on trajectories looks similar.

We investigated the particle trajectories for a wide variety of the η_0 parameters. Three types of trajectories can be seen for all investigated cases $\eta_0 < 1$. Oscillating trajectories are more probable for $\eta_0 \ll 1$, on the other hand, frozen trajectories and precipitation trajectories are to keep its relative width independently of parameter η_0 . Summary of these results are pre-

Table 1. The critical parameters of the trajectories.

η_c	$\alpha_{e,os}$	$\alpha_{e,fl}$	$\gamma_{e,end,max}$
1.25×10^{-5}	0.037	0.021	17.42
1.25×10^{-4}	0.080	0.041	29.65
1.25×10^{-3}	0.153	0.081	50.44
1.25×10^{-2}	0.288	0.162	85.60
1.25×10^{-1}	0.669	0.325	145.5
0.613	1.52	0.57	210

Table 2. For dimensionless cooling time parameter η_0 (see Eq. 2.24) and $\gamma_e \gg 10^2$ we presented critical initial pitch angles, which separated different kinds of trajectories: 1) oscillation – $\alpha_{e,0} > \alpha_{e,os}$; 2) freezing – $\alpha_{e,os} \geq \alpha_{e,0} > \alpha_{e,fl}$; 3) precipitation – $\alpha_{e,fl} \geq \alpha_{e,0}$. The maximum Lorentz factor of falling electrons is presented as $\gamma_{e,end,max}$ ($\gamma_{e,fl,max}$ measured at $\alpha_{e,0} = 0.00061$).

sented in Table 1 and Fig. 3. The critical pitch angle, which separates falling/“precipitation” trajectory can be estimated with accuracy better 1% as

$$\alpha_{e,fl} = 0.589\eta_c^{0.30}, \quad (3.3)$$

consistent with (3.2). For the “frozen” trajectory, the pitch angle should be less when

$$\alpha_{e,os} = 1.079\eta_c^{0.30}. \quad (3.4)$$

This expression works with accuracy better 1% for $\eta < 0.1$. The maximal Lorentz factor of the falling particles can be estimated as

$$\Gamma_{end} = 234\eta_c^{0.23}.$$

3.3 Injection procedure and emissivity

For the location of injected particles, we chose a particular radius and inject at various polar angles. Injection at various polar angles allows us to mimic various accretion geometries and orientations of the magnetic axis of the accelerator. For the fully aligned case, the injection is expected at magnetic equator, $\theta = \pi/2$, Figs. 7–8. In addition, we investigated the case of $\theta = \pi/8, \pi/6, \pi/4, \pi/3$ (Fig. 9).

To construct emission pasterns, we inject an ensemble of particles with uniform distribution in initial velocity direction and spectrum $dN/d\gamma_e \propto \gamma_e^{-2}$. The emission patterns are the intensity of the photon emission depends on two viewing angles relative to the WD center and magnetic axis θ and ϕ . The θ and ϕ are altitude and azimuthal angles, respectively. For the particle emission point $(\phi, \theta) = (0, \pi/2)$ emission patterns in optics and X-ray are presented on the Fig. 8, here we change η_0 parameter from 1.25×10^{-3} (top row) till 1.25×10^{-5} (bottom row). As we can see for $\eta_0 \geq 10^{-4}$ the emission pattern is simple, equatorial zone dominates in the emission and the light curve will be nearly constant if rotation axis is parallel to the magnetic one. For smaller values of the η_0 parameter we can see two distinct peaks which will form two maximum on the light curves as in optics as in X-ray. In general, light curves as in optics as in X-ray look very similar.

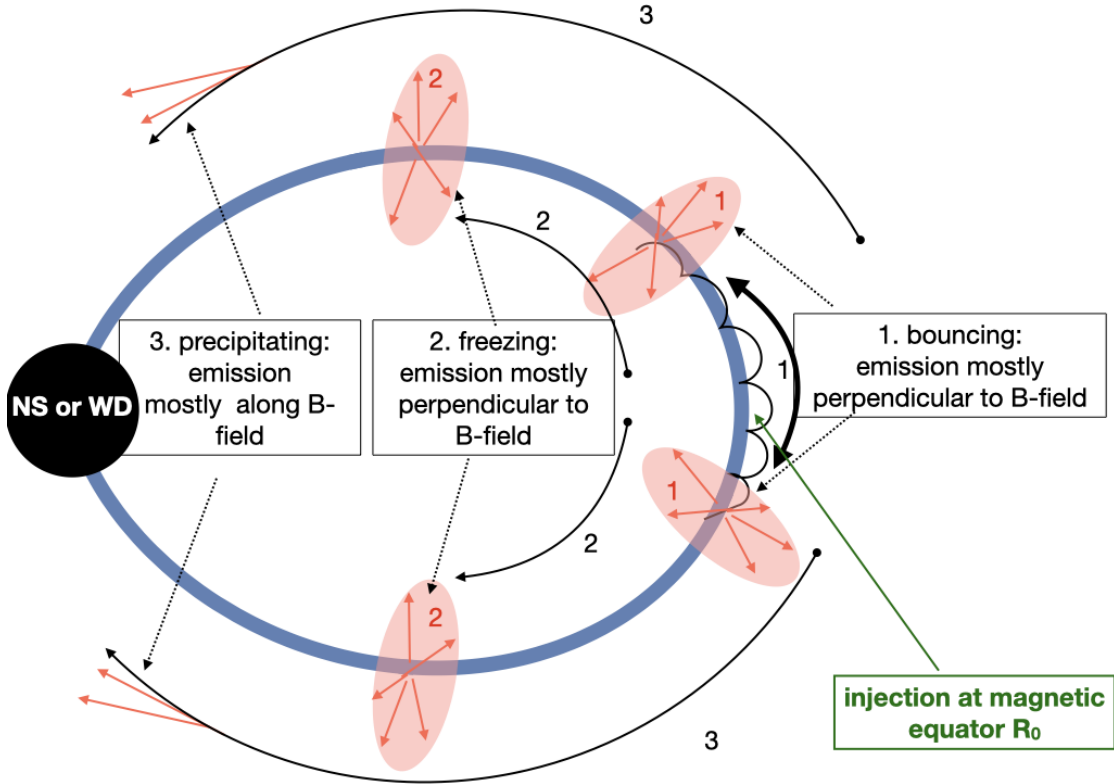


Figure 4. Cartoon of different particles' trajectories and emission patterns. In the slow cooling case (1) particles mostly bounce between reflection points producing emission mostly near the reflection point orthogonally to the magnetic field. For the freezing case (2) particles lose nearly all the energy in one go and fall to the star with small energies; emission is produced also mostly orthogonally to the magnetic field. In the case of precipitation (3) particles keep their relativistic parallel momenta, so that emission is beamed along magnetic field. Qualitatively, for our parameters, it is trajectory 1 that dominates overall emission (more particles are in this regime).

The synchrotron power of each particle can be calculated as $L_{syn} = d\gamma_e/dt$. To calculate the synchrotron, for a given Lorentz factor and pitch angle, we use the most probable frequency of

$$\nu = 0.29 \frac{3Be}{4\pi m_e c} \gamma_e^2 \sin^2 \alpha. \quad (3.5)$$

At each point, emission is beamed into a conical diagram with opening angle $\Delta \sim 1/\gamma$ around the pitch angle α , Fig. 5. When motion becomes mildly relativistic, $\gamma_e \sim \text{few}$ and the emission diagram becomes wide, the synchrotron emissivity is small.

Thus, for each particle injected with a given pitch angle α_0 and given Lorentz factor γ_e , we follow its evolution by solving system (2.27). Then at each point we calculated the intensity and direction of synchrotron emission, and project it onto the sphere of the sky.

3.4 Emission patterns and spectra

Next, we calculate the light curves and spectra of synchrotron emission. First, in Fig. 6 we show particles' trajectories in the emitted frequency - Lorentz factor plane for equatorial

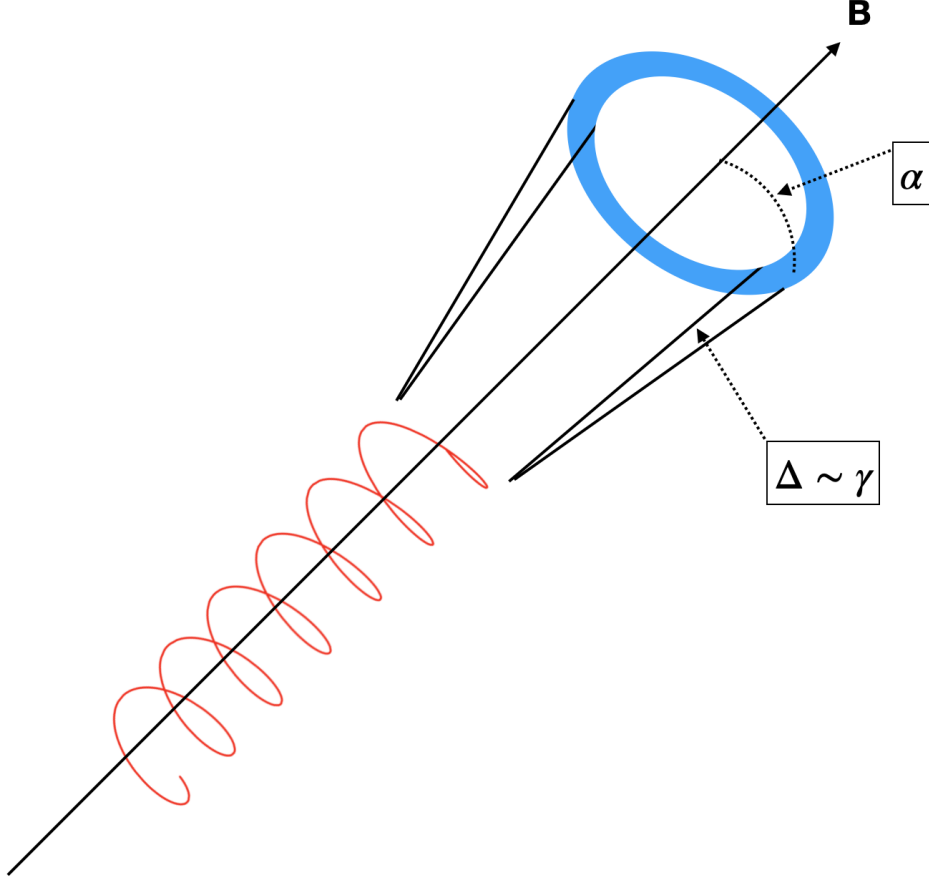


Figure 5. Emission pattern

injection. Particles first start at the highest Lorentz factors, but in a low magnetic field, so that emitted frequency is relatively low. As they propagate into stronger magnetic field, and increasing their pitch angle, the emitted frequency increases.

Spectral properties of the resulting emission are presented in Fig. 6. The Lorentz factor is the main factor, but in general the dependence is non-trivial, as less energetic particles propagating deep into the magnetosphere produce higher energy photons, while higher energy particles gyrating at a large distance produce lower frequencies. For example, for relatively large pitch angles and large Lorentz factors the emission frequency drops down due to particle oscillations at relatively large distances (see Fig. 2) and smaller magnetic field strength. For the parameters characteristic to system AR Sco at higher energies, in optics emission is produced by electrons with energy about 1 GeV and X-rays are formed by electrons with energy larger 20 GeV. Interesting that the largest part of emission is produced with high pitch angles $\alpha_e > \pi/4$, but maximum photon energy vary on factor ~ 1.5 for difference in initial pitch angles from 0.005 till 1.

On the Fig. 7 we show dependence of normalized synchrotron luminosity depends on radius (left top), Lorentz factor (right top), pitch angle (left bottom) and emission frequency (right bottom) for $\eta_0 = 1.25 \times 10^{-5}$. The luminosity is a strong function as a Lorentz factor

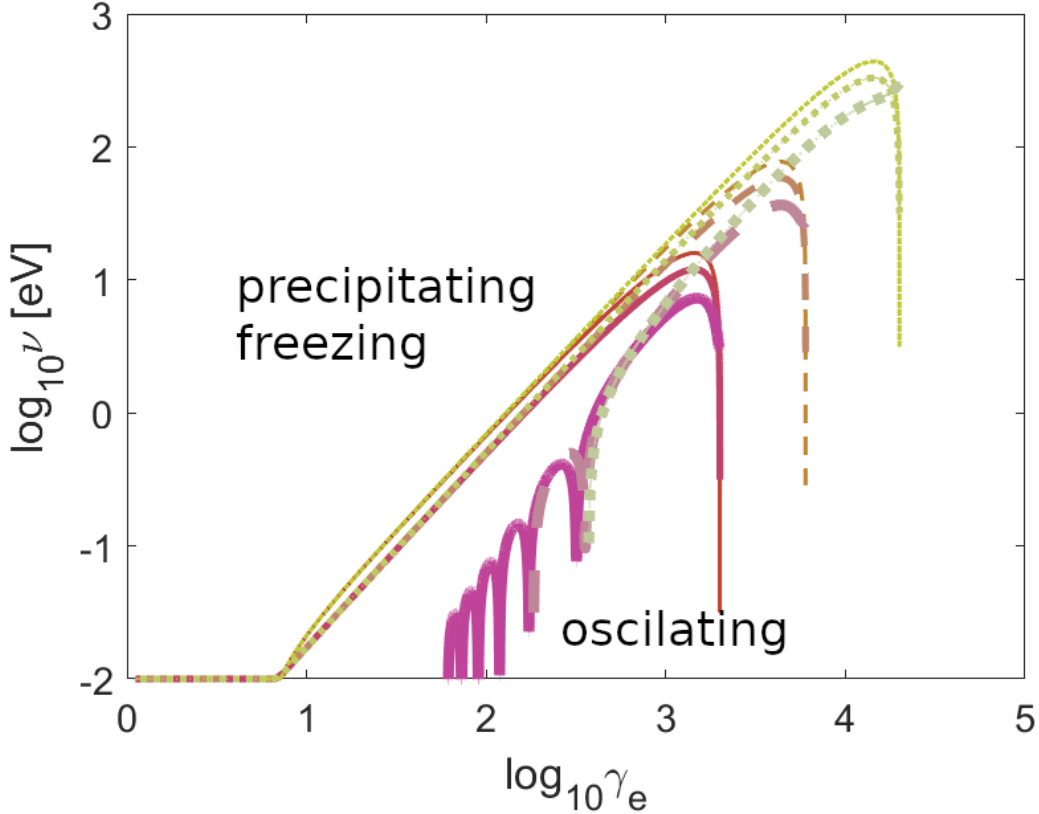


Figure 6. Trajectories of particles in the magnetosphere plotted in the “frequency – Lorentz factor” plane, equatorial injection. Lorentz factors (increasing to the right) and different pitch angles (increasing from top to bottom in each set). The thin lines corresponds to $\alpha_{e,0} = 0.005$, the medium $\alpha_{e,0} = 0.05$ and thick ones $\alpha_{e,0} = 0.5$. The solid lines corresponds to $\gamma_{e,0} = 2 \times 10^3$, the dashed $\gamma_{e,0} = 6 \times 10^3$ and dotted $\gamma_{e,0} = 2 \times 10^4$.

as a pitch angle. The higher Lorentz factor leads to grow of luminosity. The small pitch angle allows particle travel to high magnetic field region before significant loses of the initial Lorentz factor and the growth of the pitch angle in the region with high magnetic field strength leads to more bright and hard emission. Even for small value of the η_0 parameter, the main energy loss process for particle’s majority take place at relatively large heights $0.5 < r < 0.9$.

In Fig. 8 we plot sky emission maps at different photon energies and different radiation (cooling) parameter η_0 . Particles are injected only at fixed azimuthal angle $\phi = 0$. For strong cooling, $\eta \geq 10^{-4}$, particles lose most of the energy near the initial equatorial plane, while producing emission mostly in the equatorial plane. Qualitatively, top and middle rows correspond to trajectory 1 in Fig. 4.

For weaker cooling, smaller parameters η (bottom row in Fig. 8, the picture change: a particle has time to move from the equatorial plane towards the magnetic axis. As a result, emission is produced into a wider area of the sky. Yet the points $\phi = \pi/2$ $3\pi/2$ are special: a particle produces emission in those directions along the whole trajectory, so that the emission accumulates towards this direction.

The emission point can be significantly shifted relative to the magnetic equator, so we

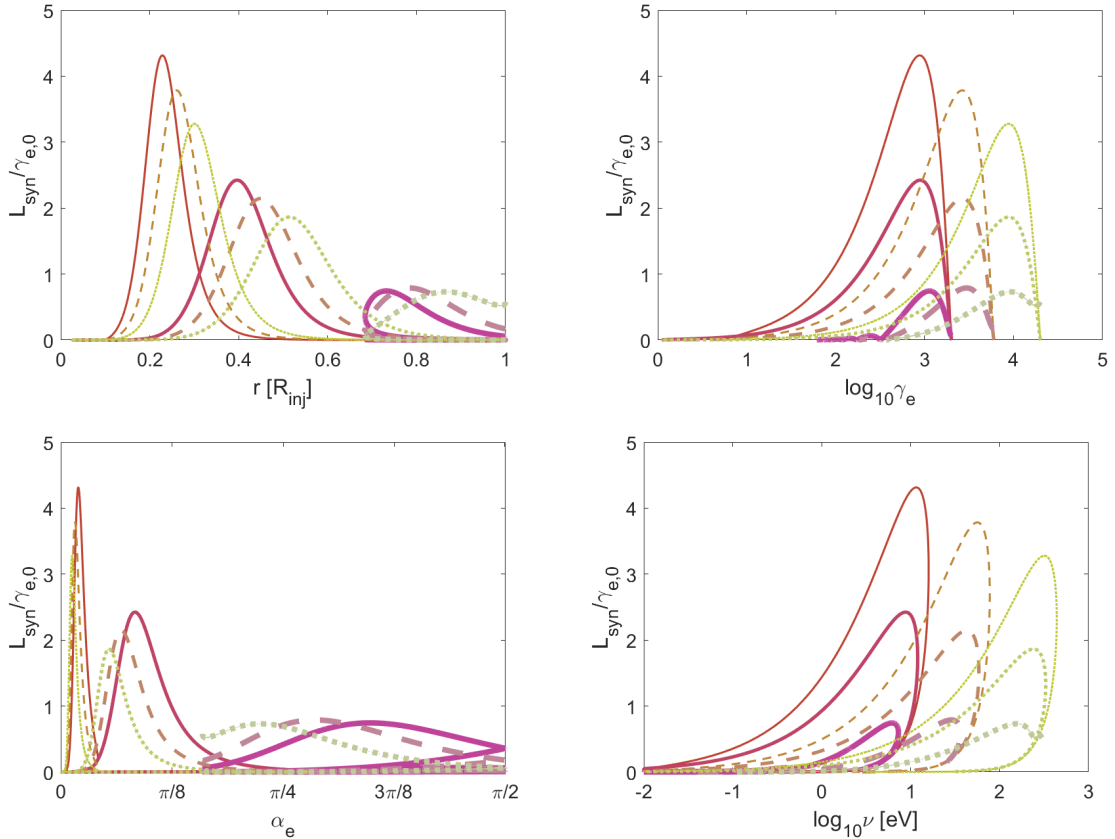


Figure 7. Equatorial injection. The synchrotron luminosity normalized on initial Lorentz factor depends on radius (top left), electron Lorentz factor γ_e (top right), pitch angle α (bottom left) and peak flux frequency of synchrotron photons ν (bottom right) are presented. The thin lines corresponds to $\alpha_{e,0} = 0.005$, the medium $\alpha_{e,0} = 0.05$ and thick ones $\alpha_{e,0} = 0.5$. The solid lines corresponds to $\gamma_{e,0} = 2 \times 10^3$, the dashed $\gamma_{e,0} = 6 \times 10^3$ and dotted $\gamma_{e,0} = 2 \times 10^4$.

plot emission patterns for different emission points on the Fig. 9 for $\eta_0 = 1.25 \times 10^{-4}$. As we can see, the light curve can have two peaks or be quite faint. We should note, what the distance between peaks can vary in wide range from π up to 0—complete merge. Also for nonsymmetrical injection point the slopes of the light-curve are different (not symmetric) and if one have fast-rise slow decay the second will have slow-rise and fast-decay, such combination take place if injection point in opposite hemisphere compare to direction to observer. The opposite combination of rise -decay is also possible.

In Fig. 9 we investigate various injection locations $\theta_c = \pi/3; \pi/4; \pi/6; \pi/8$. For injection closer to the axis (smaller θ_c) particles experience strong in one-go. Their emission pattern is affected by mildly relativistic parallel velocity. Qualitatively, this corresponds to trajectory 2 in Fig. 4.

4 Applications and discussion

Our results have direct implementation to the observed properties of the intermediate polars.

The direct heating by synchrotron photons un able to form observed compact polar hotspots on the WD [15]. On the over hand, the frozen electrons with small initial pitch

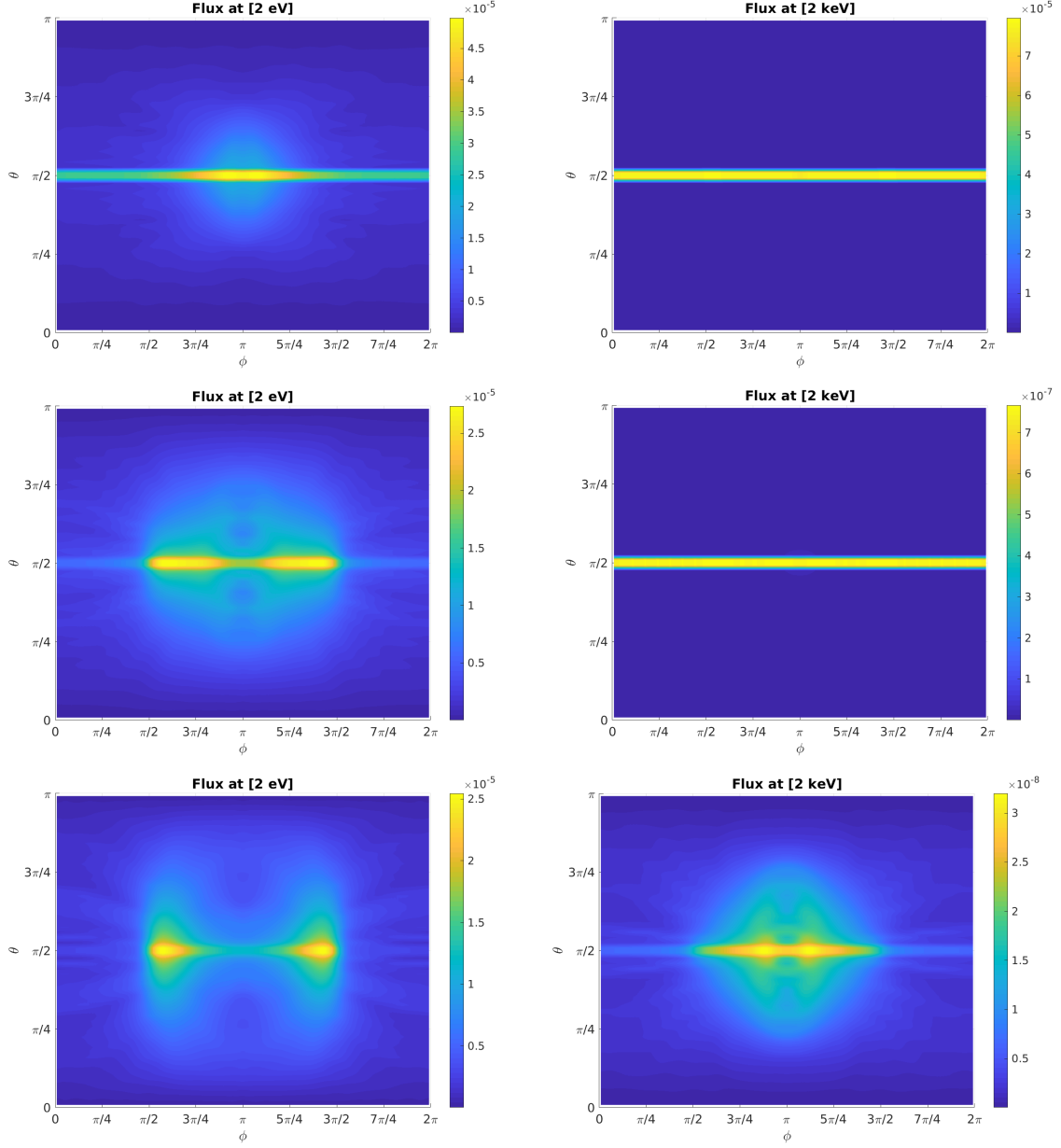


Figure 8. The synchrotron luminosity maps in optical (left) and in X-ray (right) energy band depends on viewing angle (θ, ϕ) . Here $\theta = 0$ in direction of magnetic axis, $\phi = 0$ in direction of magnetic field line plane, and the injection point $(\theta, \phi) = (\pi/2, 0)$. The η_0 was varied in the range 1.25×10^{-3} top row, 1.25×10^{-4} middle row and 1.25×10^{-5} bottom row.

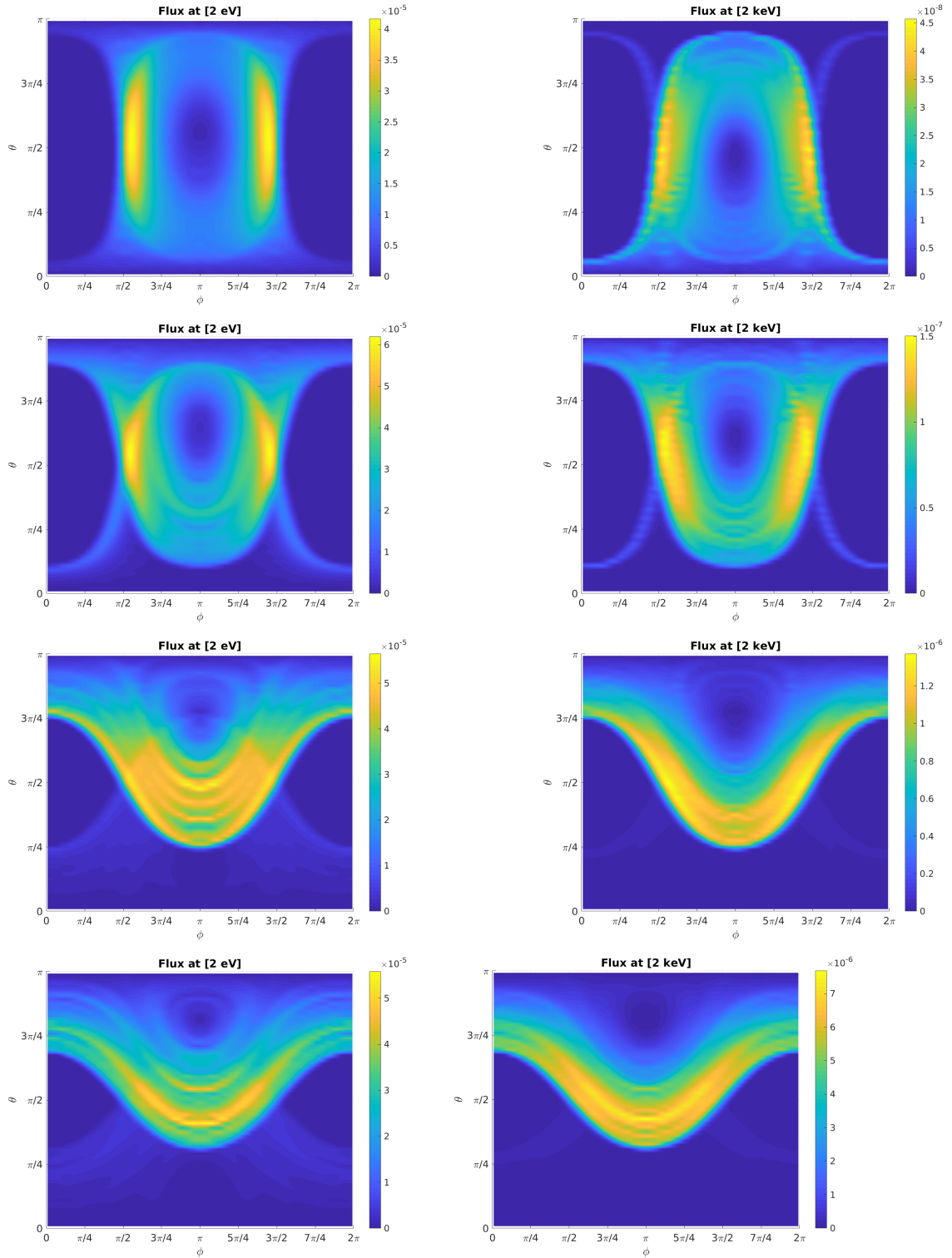


Figure 9. Synchrotron Emission maps for various injection locations $\theta_c = \pi/3; \pi/4; \pi/6; \pi/8$ from top to bottom. The synchrotron luminosity maps in optical (left) and in X-ray (right) energy band depends on viewing angle (θ, ϕ) . Here $\theta = 0$ in direction of magnetic axis, $\phi = 0$ in direction of magnetic field line plane. For the $\eta_0 = 1.25 \times 10^{-4}$.

angle can penetrate deep into magnetosphere and heat the polar hats of the WD as it is discussed in the [15].

An interesting point which we get in our calculations is the maximal emission take place at quite large pitch angles (see Fig. 7, $\alpha \sim \pi/4$), so the emission cone is wide for the majority of particles. It can be relatively narrow (~ 0.1) only for small initial pitch angles, indeed ($\alpha < 0.01$). We can say that for small initial pitch angles, the emissivity cone will be at least an order of magnitude wider when initial ones [but see simplified approach in 16].

We can describe several possible configurations and characteristic pulse profile behavior.

- *Magnetic moment parallel to the rotation axis and injection is in equatorial plane:* The light curve can have single peak ($\eta_e > 10^{-3}$) or close to constant emission, especially in hard energy range.
- *Magnetic moment parallel to the rotation axis, but injection point varies depends on orbital phase:* depends on observer position light curve can vary from two distinct peaks with smooth deep in between till no signal (weak signal) or narrow single peak. In the case of strong inclination of injection point, the peaks can "merge" to single wide one with steep rise and decay
- *Magnetic moment not parallel to the rotation axis, and injection point varies depends on orbital phase:* The light curve can have two different in intensity peaks. The peaks should be asymmetric, with relatively shallow fronts between them and steep profiles for opposite fronts.

Acknowledgments

BMV appreciate for partial support BASIS foundation grant #24-1-2-25-1.

References

- [1] S.-I. Akasofu and S. Chapman, The Ring Current, Geomagnetic Disturbance, and the Van Allen Radiation Belts, [*Geophys. Res.* **66** \(1961\) 1321](#).
- [2] H. Alfven, Cosmical electrodynamics (1950).
- [3] M. Lyutikov and C. Thompson, Magnetospheric Eclipses in the Double Pulsar System PSR J0737-3039, [*ApJ* **634** \(2005\) 1223](#) [[astro-ph/0502333](#)].
- [4] D.A.H. Buckley, P.J. Meintjes, S.B. Potter, T.R. Marsh and B.T. Gänsicke, Polarimetric evidence of a white dwarf pulsar in the binary system AR Scorpii, [*Nature Astronomy* **1** \(2017\) 0029](#) [[1612.03185](#)].
- [5] B. Marcote, T.R. Marsh, E.R. Stanway, Z. Paragi and J.M. Blanchard, Towards the origin of the radio emission in AR Scorpii, the first radio-pulsing white dwarf binary, [*AAP* **601** \(2017\) L7](#) [[1705.00600](#)].
- [6] M. Lyutikov, M. Barkov, M. Route, D. Balsara, P. Garnavich and C. Littlefield, Magnetospheric interaction in white dwarf binaries AR Sco and AE Aqr, [arXiv e-prints \(2020\)](#) [[arXiv:2004.11474](#)] [[2004.11474](#)].
- [7] A. Papitto, D.F. Torres and J. Li, A propeller scenario for the gamma-ray emission of low-mass X-ray binaries: the case of XSS J12270-4859, [*MNRAS* **438** \(2014\) 2105](#) [[1312.0456](#)].

- [8] A. Papitto and D.F. Torres, A Propeller Model for the Sub-luminous State of the Transitional Millisecond Pulsar PSR J1023+0038, [ApJ](#) **807** (2015) 33 [1504.05029].
- [9] J.W. Dungey, Loss of Van Allen electrons due to whistlers, [Planet. Space Sci.](#) **11** (1963) 591.
- [10] B. Abel and R.M. Thorne, Electron scattering loss in Earth's inner magnetosphere 1. Dominant physical processes, [Geophys. Res.](#) **103** (1998) 2385.
- [11] F.V. Coroniti, Energetic Electrons in Jupiter's Magnetosphere, [ApJS](#), **27** (1974) 261.
- [12] R.B. Horne, R.M. Thorne, Y.Y. Shprits, N.P. Meredith, S.A. Glauert, A.J. Smith et al., Wave acceleration of electrons in the Van Allen radiation belts, [Nature](#) **437** (2005) 227.
- [13] L.D. Landau and E.M. Lifshitz, The classical theory of fields (1975).
- [14] L.F. Shampine and M.W. Reichelt, The matlab ode suite, [SIAM Journal on Scientific Computing](#) **18** (1997) 1 [<https://doi.org/10.1137/S1064827594276424>].
- [15] P. Garnavich, C. Littlefield, M. Lyutikov and M. Barkov, Peeking Between the Pulses: The Far-UV Spectrum of the Previously Unseen White Dwarf in AR Scorpii, [ApJ](#) **908** (2021) 195 [2012.09868].
- [16] L. du Plessis, C. Venter, Z. Wadiasingh, A.K. Harding, D.A.H. Buckley, S.B. Potter et al., Probing the non-thermal emission geometry of AR Sco via optical phase-resolved polarimetry, [MNRAS](#) **510** (2022) 2998 [2112.08708].